OPEN ACCESS
IOP Publishing | International Atomic Energy Agency
Nuclear Fusion
Nucl. Fusion **65** (2025) 036029 (16pp)
https://doi.org/10.1088/1741-4326/adb442

Designing a validation experiment for radio frequency condensation

Lanke Fu[1,*], E. Litvinova Mitra[1], R. Nies[2], A.H. Reiman[2], M. Austin[3], L. Bardoczi[4], M. Brookman[5], Xi Chen[6], W. Choi[6], N.J. Fisch[2], Q. Hu[2], A. Hyatt[6], E. Jung[2], R. La Haye[6], N.C. Logan[7], M. Maraschek[8], J.J. McClenaghan[6], E. Strait[6], A. Welander[6], J. Yang[2] and the ASDEX Upgrade Team[8,a]

[1] Princeton University, Princeton, NJ, United States of America
[2] Princeton Plasma Physics Laboratory, Princeton, NJ, United States of America
[3] University of Texas, Austin, TX, United States of America
[4] University of California, Irvine, CA, United States of America
[5] Commonwealth Fusion Systems, Boston, MA, United States of America
[6] General Atomics, La Jolla, CA, United States of America
[7] Columbia University, New York, NY, United States of America
[8] Max Planck Institute for Plasma Physics, Garching, Germany

E-mail: lankef@princeton.edu

Received 26 August 2024, revised 17 January 2025
Accepted for publication 10 February 2025
Published 19 February 2025

Abstract

Theoretical studies have suggested that nonlinear effects can lead to 'radio frequency (RF) condensation', where an initially broad current profile can coalesce in islands when they reach sufficient width. In suitable conditions, RF condensation can 'self-focus' the driven current to the center of an island, improving stabilization efficiency and reducing control complexity. In unsuitable conditions, the effect can prematurely deplete the RF energy before it reaches the island center, impairing stabilization. It is predicted that the RF condensation effect can significantly impact reactor-scale tokamaks. This paper presents a set of simulations investigating the conditions under which RF condensation might be encountered in present-day tokamaks. For concreteness, the calculations use equilibrium reconstructions for two shots from DIII-D and AUG. The Current Condensation Amid Magnetic Islands (OCCAMI) simulation code has been used for this investigation. The code takes as its input a numerically specified axisymmetric EFIT equilibrium solution, and it perturbatively constructs a 3D field with an island embedded at the appropriate rational surface. In the OCCAMI code, the GENRAY code is used for ray tracing and for calculating the power deposition along a ray trajectory, and GENRAY is coupled self-consistently to a solution of the thermal diffusion equation in the island. The simulation results described in the paper illuminate the conditions required for experimental validation of the theory of RF condensation. The simulations also provide an explanation of why the effect was not noticed in experiments prior to the publication of theoretical papers on the subject.

[a] See Zohm *et al* 2024 (https://doi.org/10.1088/1741-4326/ad249d) for the ASDEX Upgrade Team.
[*] Author to whom any correspondence should be addressed.

Keywords: magnetic islands, tearing modes, electron cyclotron waves

(Some figures may appear in colour only in the online journal)

1. Introduction

Disruptions pose a serious threat to the tokamak fusion program. The Joint European Torus (JET), which was the largest operating tokamak in the international fusion program from 1983 to 2023, has provided valuable data on disruptions. In particular, it has been found that the growth of large islands precedes 95% of the disruptions in JET with the ITER-like wall [1]. Although these islands generally appear at the end of a chain of other off-normal events, it appears that it is the island itself that typically triggers the disruption [2]. A statistical analysis of 250 disruptions on JET found a distinct locked mode amplitude at which the plasma disrupted, corresponding to an island width of about 30% of the minor radius [3]. A method for automatically stabilizing such islands would clearly be desirable.

Theoretical investigations in the late 1970s showed that radio frequency (RF) waves could be used to drive plasma currents [4, 5]. Subsequent theoretical investigations in the early 1980s showed that it would be feasible, and desirable, to stabilize magnetic islands using those RF-driven currents [6, 7]. Since that time, RF current drive stabilization of magnetic islands has been extensively demonstrated experimentally [8–15].

Recent theoretical studies have found that RF condensation, a nonlinear effect not included in conventional RF calculations, may significantly impact island stabilization [16–29]. RF condensation arises from the sensitivity of the RF power deposition and driven current to temperature perturbations. A temperature perturbation in an island increases the local power deposition, which further increases the temperature perturbation. In addition, the electron cyclotron (EC) driven current is itself sensitive to the temperature perturbation, further enhancing the non-linear effect. As a result, in a magnetic island with sufficient width, the non-linear feedback can 'condense' an initially broad RF deposition and driven current profile to a small region of the island. In favorable conditions, this effect can 'self-focus' RF energy to the island center. This can potentially improve RF stabilization efficiency and simplify launcher feedback control [20, 21, 24]. In unfavorable conditions, RF condensation may prematurely deplete the RF energy before it reaches the island center. When not accounted for, this can impair island stabilization below the level predicted by conventional calculations. Recent calculations show that RF condensation is relevant in both ITER [21, 23] and ARC-like conditions [30]. Experimental validation of the RF condensation effect is therefore critical to the design and operation of reactor-class tokamaks.

This paper presents a set of simulations investigating the conditions under which RF condensation might be encountered in present-day tokamaks. For concreteness, the calculations use equilibrium reconstructions for two shots from DIII-D and AUG. The simulation results illuminate the conditions required for experimental validation of the theory of RF condensation. The results also provide an explanation of why the condensation effect was not noticed in experiments prior to the publication of theoretical papers on the subject.

Our simulations use the Of Current Condensation Amid Magnetic Islands (OCCAMI) [23] code. The code takes a numerically specified axisymmetric equilibrium as input, and it perturbatively constructs a 3D field with an island of specified width embedded at the appropriate rational surface [31]. We use reconstructed experimental equilibria from DIII-D and ASDEX Upgrade (AUG), specifically for shot 141 060 on DIII-D and shot 35 350 on AUG. DIII-D shot 141 060 has been previously used in an experiential study of the electron cyclotron current drive (ECCD) stabilization of locked islands [25]. The DIII-D calculations make use of top launchers at the locations where such launchers were installed on DII-D. The AUG calculations use only outside launchers, i.e. launchers on the low field side of the tokamak.

Figure 1 shows a cross-section of a 3D equilibrium constructed in OCCAMI from a reconstructed 2D equilibrium for shot 141 060. An example ray trajectory is shown. OCCAMI iterates between the ray-tracing code, GENRAY [32], and a thermal diffusion equation solver to self-consistently calculate the non-linear amplification of island temperature due to RF condensation. During each iteration, OCCAMI first calculates the trajectories and deposition of the EC waves with GENRAY. OCCAMI then solves a thermal diffusion equation in the islands to update the temperature and density profiles in the islands, using the GENRAY deposition as the source terms. The updated profile is fed back to GENRAY for the next iteration, and the iteration continues until the island temperature profile converges. This allows OCCAMI to identify non-linear effects neglected by existing codes.

The key uncertainties in the theory of RF condensation relate to the nonlinear enhancement of the temperature perturbation in the island. The ECCD efficiency for a given plasma temperature and density has been well validated experimentally [33]. This paper will therefore focus on the effect of EC power deposition on the temperature perturbation in an island.

This paper will be organized as follows. Section 2 provides theoretical background. Section 3 provides additional details on the OCCAMI simulation code. Section 4 discusses relevant diagnostic challenges. Section 5 discusses the DIII-D calculations. Section 6 examines one of the DIII-D B_{tor} scans in greater detail. Section 7 discusses the AUG calculations. Section 8 discusses the conditions governing the magnitude

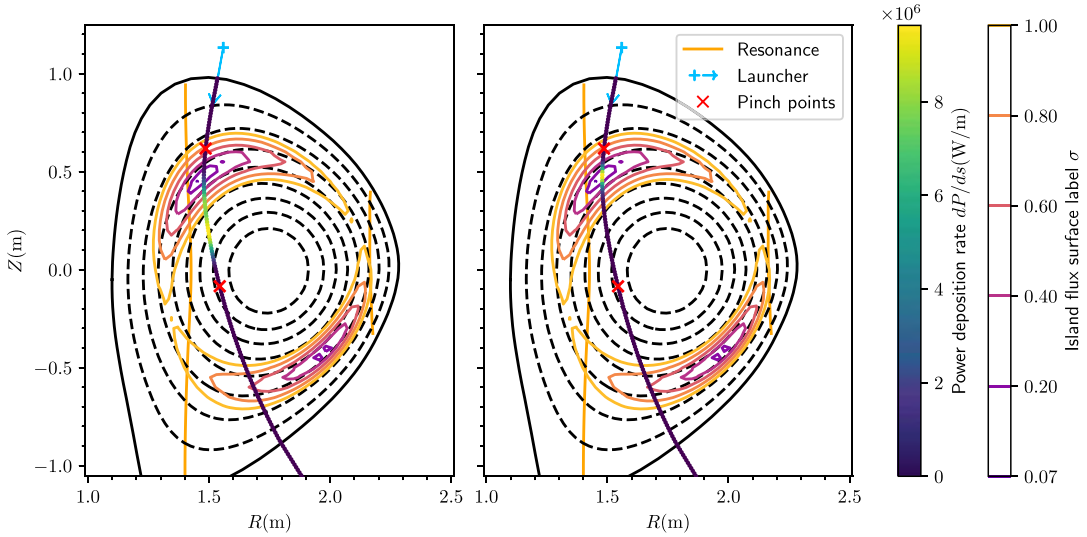

Figure 1. Linear (left) and nonlinear (right) solution for the power deposition along a top launch ray trajectory in DIII-D as calculated by the OCCAMI code.

of the nonlinear effects as seen in our calculations. Finally, section 9 discusses the results and some conclusions.

2. Theoretical background

2.1. Power deposition

EC waves in a tokamak generally deposit their energy on the tail of the electron distribution function, where the number of electrons is sensitive to the temperature of the bulk electrons. In a magnetic island, the sensitivity of the power deposition to the temperature perturbation, combined with the local thermal insulation associated with the island, causes a further increase in the temperature. This is the nonlinear feedback effect, discussed in the introduction, that is the key to RF condensation.

If the EC waves dominantly deposit their power at a phase velocity V_p, then the number of resonant electrons, and the power deposition, is roughly given by

$$\mathrm{d}P_{\mathrm{dep}}/\mathrm{d}s \propto \exp\left(-w^2\right), \tag{1}$$

where $w = V_p/V_T$ and V_T is the thermal velocity. The EC deposition rate is exponentially sensitive to small temperature perturbations $\widetilde{T}$:

$$\mathrm{d}P_{\mathrm{dep}}/\mathrm{d}s \propto \exp\left(-w_{\mathrm{eff}}^2\right)\exp\left(w_{\mathrm{eff}}^2\frac{\widetilde{T}}{T_0}\right), \tag{2}$$

where w_{eff} and T_0 are the initial values of w and T before the perturbation. This argument has been put on a firmer footing in [23].

The coalescence effect associated with RF condensation is, in some circumstances, strongly constrained by relativistic effects. Those effects constrain the power deposition to lie in the region where:

$$n\Omega/\omega \geqslant \sqrt{1-N_\parallel^2}, \tag{3}$$

$$N_\parallel = ck_\parallel/\omega. \tag{4}$$

Here, Ω is the EC frequency, n specifies the relevant harmonic, ω is the wave frequency, c is the speed of light $k_\parallel$ is the parallel wave number, and $N_\parallel$ is the parallel refractive index. [33] The bounding points of the region where this condition is satisfied are called 'pinch points'. When relativistic effects restrict the power deposition to a narrow region, that can prevent the RF from coalescing. The red crosses in figure 1 correspond to the pinch points along the ray trajectory. Power can be deposited only between those pinch points.

2.2. Heat transport in the island

There is experimental [34–36] and computational [37] evidence that the diffusion coefficient in a magnetic island is much smaller than the ambient thermal diffusion coefficient in the surrounding plasma when the temperature and density gradients in the island are small. This is plausible, as it may be expected that the small gradients would be below the threshold for triggering microinstabilities.

We assume that the transport in the island is determined by ion temperature gradient (ITG) modes. To reflect this, we use a conventional model for the effect of the ITG threshold on the thermal diffusion coefficient [38]:

$$\kappa_\perp = \begin{cases} \kappa_0 & \left(-\frac{R}{T}\frac{dT}{dr} < k_c\right) \\ \kappa_0\left[1+\frac{\kappa_s}{\kappa_0}\left(-\frac{R}{T}\frac{dT}{dr}-k_c\right)\right] & \left(-\frac{R}{T}\frac{dT}{dr} \geqslant k_c\right) \end{cases} \tag{5}$$

where κ_0 is the thermal diffusivity below the ITG threshold, k_c is the normalized ITG threshold, R is the major radius and κ_s/κ_0 is a measure of the stiffness.

For the values of the parameters in equation (5), we consider the experimental data presented in [38] The values of k_c vary over a relatively narrow range, from 3 to 8, with 5 or 6 being a reasonable average value. The values of κ_s/κ_0 vary over a relatively broad range. As a reasonable average value, we take κ_s/κ_0 to be 3.0 in the following. In practice, the choice of the κ_s parameter within the observed range does not significantly impact our conclusions in this paper, because the profiles become sufficiently stiff that it becomes much more difficult to extract useful data concerning RF condensation once the k_c threshold is exceeded. Finally, experiments have indicated that κ_0 is at least an order of magnitude smaller than the thermal diffusivity outside the island, where the diffusivity κ_0 is approximately $1\,\mathrm{m}^2\,\mathrm{s}^{-1}$. We therefore take $\kappa_0 = 0.1\,\mathrm{m}^2\,\mathrm{s}^{-1}$. For the values of the parameters in equation (5), we consider the experimental data presented in [38] The values of k_c vary over a relatively narrow range, from 3 to 8, with 5 or 6 being a reasonable average value. The values of κ_s/κ_0 vary over a relatively broad range. As a reasonable average value, we take κ_s/κ_0 to be 3.0 in the following. In practice, we will see that the choice of this parameter does not significantly impact our conclusions in this paper. Once the ITG threshold is exceeded, the profiles become sufficiently stiff that it becomes much more difficult to extract useful data concerning RF condensation. Finally, experiments have indicated that this κ_0 is at least an order of magnitude smaller than the thermal diffusivity outside the island, where the diffusivity κ_0 is approximately $1\,\mathrm{m}^2\,\mathrm{s}^{-1}$. We therefore take $\kappa_0 = 0.1\,\mathrm{m}^2\,\mathrm{s}^{-1}$.

The calculations for this paper have used a single fluid model. Experiments in AUG and W7X have found that, depending on the electron-ion collision frequency, the electron temperature can significantly exceed the ion temperature when the ion temperature is clamped near the ITG threshold. The electrons are affected indirectly by the ITG clamping through their coupling with the ions. This suggests that experiments may produce stronger non-linear effects than predicted by our calculations.

For a table of important physical quantities, see appendix A.

2.3. Launcher location and impacts

This paper covers possible scenarios with EC waves launched above the plasma ('top launch') and from the low field side of the plasma ('outside launch').

Most tokamak experiments with EC waves have been done with outside launch. Outside launch current drive efficiency is highest at intermediate toroidal launch angles, and the capability of outside launchers to launch waves at large toroidal launch angles tends to be limited. (See section 7 and figure 13 for a further discussion of these issues.)

Although technically more difficult to implement, top launch ECCD has higher current drive efficiency than outside launch, and therefore more likely to be used in tokamak reactors, to reduce the recirculating power. DIII-D has completed top launch ECCD experiments at large toroidal launch angles [39, 40]. For the purposes of this study, top launch is of particular interest because the nonlinear effects are the most pronounced at large toroidal launch angles.

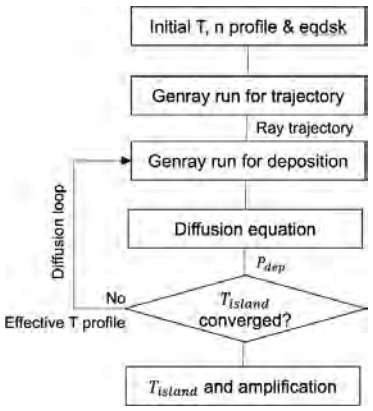

Figure 2. OCCAMI flow chart.

The upper EC launcher on ITER may be regarded as intermediate between top launch and outside launch, with the EC beam launched from above the plasma, but from a major radius larger than that at the magnetic axis ($R = 7$ m, $z = 4.2$ and 4.4 m).

3. The OCCAMI simulation code

Our simulations employ the numerical code OCCAMI [23], which iterates between the GENRAY geometrical optics ray tracing code [32] to evaluate the island power deposition and a diffusion equation solver for the island temperature profile. The code uses a numerically specified equilibrium file produced by the EFIT code [41]. The rational surface of interest and island width are specified as input parameters. A 3D field with an island of the specified width is constructed [31]. The density and temperature are initially flattened in the island region. The density profile is kept flat. The code iterates to calculate a self-consistent temperature profile in the island with the heat source term calculated by GENRAY.

The flow of the logic in the OCCAMI code is shown in figure 2 During initialization, GENRAY calculates the ray trajectory in the initial axisymmetric equilibrium. The temperature and density profile along the trajectory are updated using the 3D perturbed flux surfaces, with flattened density and temperature in the island region. The ray trajectory and the power deposition along the trajectory are then recalculated by GENRAY using the modified density and temperature along the trajectory. The small resonant magnetic field perturbation producing the island is neglected during ray tracing. The power deposited in the interior of a given flux surface in the island is calculated by subtracting the power in the wave when it exits that region from the power in the wave when it enters that region.

To calculate the temperature perturbation in the island, we solve a thermal diffusion equation there. To obtain a diffusion

equation in magnetic island geometry, we employ a conventional cylindrical model for the magnetic field,

$$\mathbf{B} = \nabla\psi \times \hat{z} - (kr/m)B_z\hat{\theta} + B_z\hat{z}, \tag{6}$$

where we can expand ψ about the rational surface as

$$\psi = \psi_0''(r - r_s)^2/2 - \epsilon\cos(m\zeta),$$

$\zeta = \theta - kz/m$, and ϵ is a constant (the 'constant-psi approximation'). We define

$$\sigma^2 = \psi/2 + 1/2.$$

It is assumed that the temperature is constant on the flux surfaces in the island. At each iteration, the code updates the temperature profile in the island by solving the cross-field heat diffusion equation with the calculated power deposition as the source term. The diffusion equation can be analytically integrated once to reduce its order, yielding the first-order ODE,

$$\frac{\mathrm{d}u}{\mathrm{d}\sigma} = -\frac{P_{\mathrm{dep}}(\sigma)}{n\kappa_\perp T_s}\frac{\sigma}{E(\sigma) - (1-\sigma^2)K(\sigma)}\frac{WM}{32\pi r_r R_0}. \tag{7}$$

Here, $u = (T - T_s)/T_s$ is the normalized island temperature; T_s is the separatrix temperature; σ is an island radial flux surface coordinate that ranges from 0 at the O-point to 1 at the separatrix; P_{dep} is the power deposition; n is the density; E and K are are complete elliptical integrals of the first and second kind; W is a prescribed island width; M is the island poloidal mode number; R_0 is the major radius. r_r is the minor radius at the rational surface. (A detailed derivation of the equation can be found in [23].) The updated temperature profile is fed back to GENRAY to obtain the P_{dep} profile for use in the next iteration. The solution is considered to be converged when the change in the island temperature between successive iterations is sufficiently small.

The solution for the temperature obtained after the first iteration corresponds to the conventional linear solution. In the following section, we will denote the value of u at the O-point by u_0. We define an amplification factor by the ratio of the converged nonlinear value of u_0 to its linear value, $A \equiv u_0/u_0^{\mathrm{lin}}$. This will provide a measure of the strength of the nonlinear effect.

4. Diagnostic considerations

In an experiment, our goal is to measure the temperature perturbation in the magnetic island. We plan to use ECE for this purpose, which has been shown to provide well-resolved measurements of temperature perturbations in magnetic islands [36, 42]. There is a complication for shot 141 060 that the field is sufficiently low that the ECE emitted at the 2nd harmonic surface encounters the third harmonic surface before exiting the plasma. Some of the power is absorbed at the third harmonic surface, and emission from the third harmonic surface pollutes the signal. A method has previously been developed to correct for this using a 1D radiation transport model [43]. For the purpose of measuring the temperature in a rotating island, there is an advantage that the ECE signal produced by the temperature perturbation in the island is time-dependent, while the ECE emitted from the third harmonic surface is stationary. This allows the development of an improved method for reconstructing the temperature perturbation in a rotating island [44].

In shot 141 060, the island locked at about 1750 ms. The above discussion suggests that it is advantageous for diagnostic purposes to maintain the rotation of the island. This can be done by entraining the island in a rotating RMP. Choi *et al* [26] describe how such an island can be entrained at 70 Hz using feed-forward entrainment.

We will see below that the nonlinear response of rotating islands to ECCD is reduced, relative to the response of locked islands. The broader power deposition in rotating islands causes the outermost flux surfaces in the island to more rapidly exceed the microinstability threshold, with the boundary of the region where the threshold is exceeded gradually moving in towards the center of the island.

5. Calculations for DIII-D

5.1. Simulation setup for DIII-D

For the DIII-D reference equilibrium, we use the reconstructed equilibrium for DIII-D shot 141 060 at 1735 ms. The plasma cross-section and the density and temperature profiles are shown in figure 3. The separatrix temperature $T_s = 1.235$ keV. During the shot, the islands lock shortly after $t = 1735$ ms. This allows us to use the same equilibrium for both the rotating and locked islands, and it provides a comparison of the nonlinear effects in a locked island with those in a rotating island. The shot was part of the 2015 DIII-D experiment studying RF stabilization of locked islands. [25] In this paper, we consider islands having widths of 20% and 25% of the minor radius.

We initialize our ray trajectories at the locations of the top launchers installed in DIII-D, $R = 1.559\,\mathrm{m}, Z = 1.133\,\mathrm{m}, \phi = 90°$ and 300°. The toroidal and poloidal launch angles of the top launchers are, $\alpha = 241°$ (0° points to $+\hat{R}$ and 90° points to $+\hat{\phi}$), and $\beta = 162°$ (0° points to $+\hat{Z}$ and 90° points to $-\hat{R}$) [40]. The launchers were installed with fixed launch angles. In the absence of the ability to steer the launch angles, we adjust the strength of the toroidal field B_{tor} to control the deposition profiles. This shifts the location of the second harmonic resonance, and thus the location of the power deposition. (Second harmonic X-mode heating is used, with the launchers operating at 110 GHz.)

For the simulations, as B_{tor} was modified, the current density was correspondingly modified to approximately preserve the q profile. The temperature and density profiles were not modified. EFIT was used to recalculate the equilibrium for each new value of B_{tor} for which a simulation was performed.

Our simulations use toroidal field direction $B_{\mathrm{tor}} > 0$ (counterclockwise when viewed from above), for which the launch

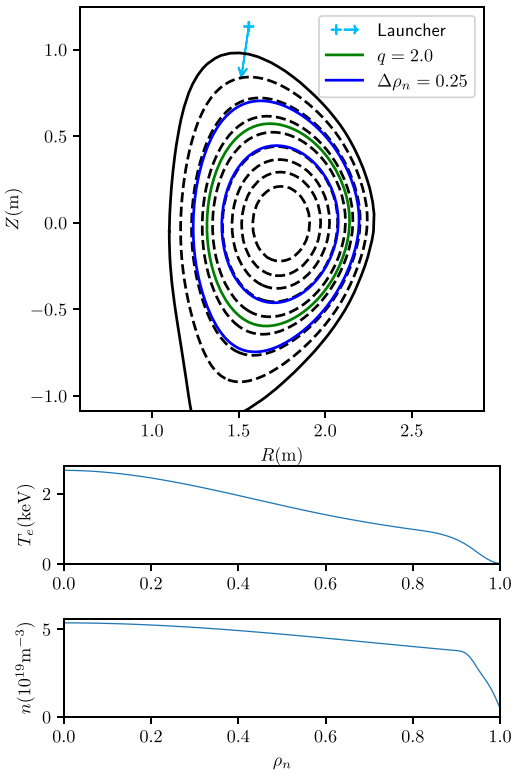

Figure 3. EFIT reconstructed equilibrium and profiles for shot DIII-D 141 060 at $t = 1735$ ms.

angles were optimized. For a table of important parameters in the numerical study, see appendix A.

5.2. Sweeps in B_{tor}

For the experiment, we propose to scan over a range of values of B_{tor} by continuously varying the current in the toroidal field coil and observe the island temperature perturbation, primarily with ECE diagnostics. This would be done for several different magnitudes of the EC power. At relatively low power, we expect the dependence of the temperature perturbation on the power to be linear, except when the microinstability threshold is encountered. When the temperature gradient is below the threshold, the non-linearity in the temperature response measures the strength of RF condensation.

We use the OCCAMI code to calculate the predicted temperature perturbation as a function of B_{tor}. Figure 4 shows a set of B_{tor} scans with 1MW of injected EC power. Figures 4(a)–(c) show the results of calculations for a locked island whose width is 25% of the minor radius. Here u_0 is the value of $u = (T - T_s)/T_s$ at the island O-point. Figure 4(a) shows the linear solution for u_0 vs. B_{tor}, while figure 4(b) shows the nonlinear solution. Every curve in each plot corresponds to a different value of the microinstability threshold parameter. The curves are identical below the thresholds. The power deposited in the island increases as B_{tor} increases. When the power deposition is small, the effect of the nonlinearity is small. As the power deposition increases, the nonlinear solution increases more rapidly. There is a discontinuous decrease in the slope when the microinstability threshold is encountered.

Figure 4(c) shows the amplification factor $A \equiv u_0/u_0^{\mathrm{lin}}$ for the 25% island. There is a narrow region just below the ITG threshold where the amplification is rapidly increasing.

In practice, we expect to see a transition from the nonlinear B_{tor} dependence of figure 4(b) to the linear dependence of 4(a) as we decrease the EC input power. (We linearly rescale the lower power measurements for comparison with the higher power.) The range of B_{tor} just below the ITG threshold will be of greatest interest. After seeing the u_0 dependence shown in 4(b), we will want to narrow the range of B_{tor} in subsequent shots to examine this region more closely.

Figure 4(d) shows the calculated amplification for a locked 20% island. The magnitude of the amplification is smaller than that for a 25% island, but the shape of the amplification vs. B_{tor} curve is approximately the same.

Figure 4(e) shows the amplification curve for a rotating island whose width is 25% of the minor radius. The decrease in the amplification is accounted for to some extent by the fact that more of the power is now being deposited outside the island. However, the shape of the curve is quite different from that for the locked islands. This is explained by the fact that a larger fraction of the power is deposited near the periphery of the island. The temperature gradient on the peripheral island flux surfaces encounters the microinstability threshold before the flux surfaces that are closer to the center. The island enters the stiff regime more gradually, with the boundary of the region where the flux surfaces encounter the threshold moving gradually inward.

Figure 4 shows the amplification curve for a rotating 20% island. The magnitude of the amplification is smaller than that for a 25% island, but the shape of the curve is approximately the same.

5.3. Bifurcation and hysteresis

Under suitable circumstances, nonlinear effects from RF condensation can produce a bifurcation of the solution to the nonlinear steady-state thermal diffusion equation. This bifurcation has two diagnostic signatures: a discontinuous jump in the temperature, or a hysteresis when a launcher parameter continuously rises above, and then returns below the discontinuity threshold. Experimentally, a sufficiently strong hysteresis can serve as an alternative signature to the nonlinear temperature growth discussed in section 5.2. Numerically, hysteresis is the preferable evidence for bifurcation, because it is impossible to distinguish between a rapid increase in u_0 with a true discontinuity due to the finite resolution of configuration scans.

We demonstrate the possibility of experimentally producing a temperature bifurcation at DIII-D by simulating a hysteresis due to RF condensation. Figure 5 shows a hysteresis curve for a 25% island in shot 141 060 with 3MW of injected power. As B_{tor} increases, there is a threshold

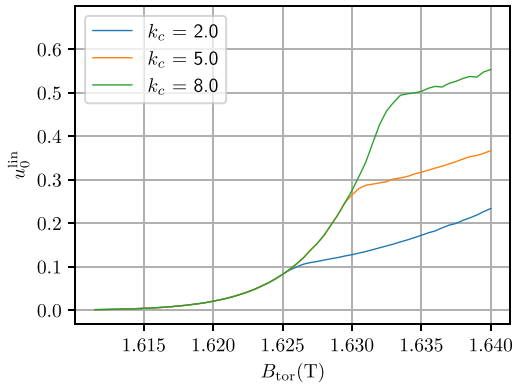

(a) Locked 25% island, linear normalized island O-point temperature perturbation u_0^{lin} vs. $B_{\rm tor}$.

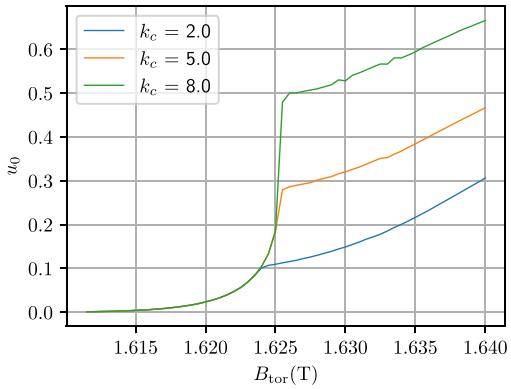

(b) Locked 25% island, nonlinear normalized island O-point temperature perturbation u_0 vs. $B_{\rm tor}$.

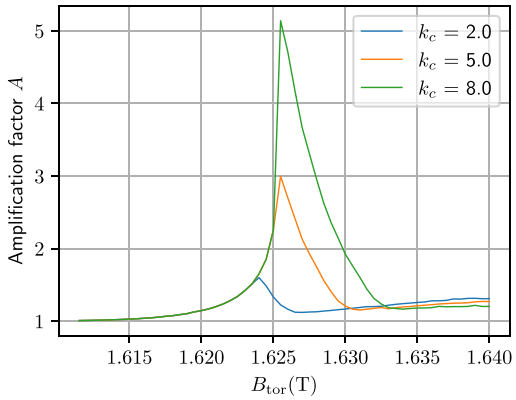

(c) Locked 25% island, amplification A vs. $B_{\rm tor}$

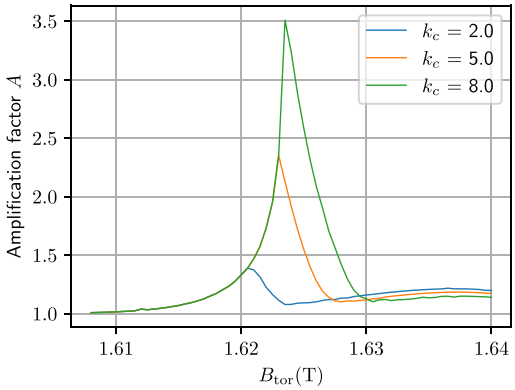

(d) Locked 20% island, amplification A vs. $B_{\rm tor}$

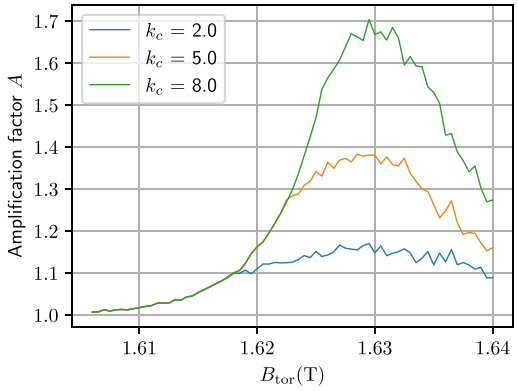

(e) Rotating 25% island, amplification A vs. $B_{\rm tor}$

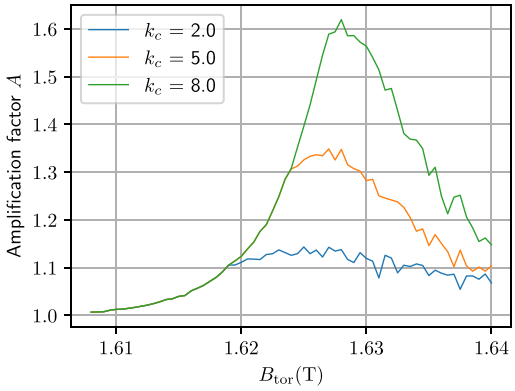

(f) Rotating 20% island, amplification A vs. $B_{\rm tor}$

Figure 4. $B_{\rm tor}$ scan results for DIII-D shot 141 060 EFIT reconstructed equilibrium with $\kappa_s/\kappa_0 = 3.0$, 1 MW of top launch EC power.

point at approximately 1.62T above which u_0 increases rapidly before encountering a discontinuous slope and a slower increase. Starting at that solution and decreasing $B_{\rm tor}$, the solution now goes past the previously encountered threshold value of $B_{\rm tor}$ for a short distance before dropping back to the previously encountered solution. Empirically, the uncertainty in toroidal magnetic field control is 0.05T. The hysteresis is likely too weak to observe experimentally. However, it is still

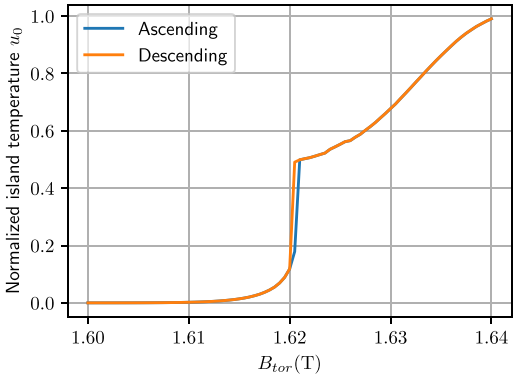

Figure 5. Hysteresis in 25% island with 3MW of EC power, $k_c = 8$, $\kappa_s/\kappa_0 = 3.0$.

of theoretical interest, because it confirms that the jump in u_0 in this configuration is indeed a true discontinuity.

6. Analysis of a DIII-D B_{tor} scan

We take a closer look at the B_{tor} scan shown in figures 4(*a*)–(*c*) for a 25% locked island with 1MW of injected EC power. Figure 6 shows plots of the amplification factor, A, the linear normalized temperature perturbation in the island, u_0^{lin}, and the nonlinear normalized temperature perturbation in the island, u_0, as a function of B_{tor}, for both the constant $\kappa_\perp$ and stiff diffusivity models. Point (*b*) corresponds to the value of B_{tor} where the constant $\kappa_\perp$ model sees the largest amplification. Point (*a*) corresponds to a slightly lower value of B_{tor}. Point (*d*) corresponds to the value of B_{tor} where the constant $\kappa_\perp$ model sees the lowest amplification. Point (*c*) corresponds to a value of b_{tor} intermediate between points (*b*) and (*d*). The values of $|B_{\mathrm{tor}}|$ at the center of the plasma for the four points (*a*), (*b*), (*c*) and (*d*) are, respectively, 1.621 T, 1.623 T, 1.639 T and 1.655 T.

Figure 7 shows w_{eff}^2 along the trajectories corresponding to each of the four points. Figures 8–11 show the plasma cross-section with w_{eff}^2, the linear power deposition, $\mathrm{d}P/\mathrm{d}s_{\mathrm{lin}}$, and the nonlinear power deposition, $\mathrm{d}P/\mathrm{d}s$, along the trajectories for each of the four points.

As B_{tor} increases, the EC resonance layer moves to larger R, closer to the ray trajectory. As a result, the peak of $P_{\mathrm{dep}}^{\mathrm{lin}}$, the power deposition predicted by the linear theory, moves earlier along the trajectory. At stage (*a*) in figure 6, the strength of the non-linear effect first gradually increases when the $P_{\mathrm{dep}}^{\mathrm{lin}}$ tail enters the island. In figure 8, we can see that the nonlinear effect is small at this stage. At stage (*b*), When $P_{\mathrm{dep}}^{\mathrm{lin}}$ at the O-point is sufficiently large, the nonlinear effect is strong, and u_0 increases rapidly with increasing B_{tor}. There is a large nonlinear shift in the position of the deposition profile along the ray trajectory, as shown in figure 9. Note that the effect of the microinstability threshold for the stiff diffusivity model causes the island temperature perturbation to saturate. The extent to which the power deposition nonlinearity affects u_0 is affected by the microinstability threshold in the island, which is unknown at present. The bulk of P_{dep} moves from the resonance to the island o-point. In stage (*c*), the further increase in B_{tor} causes the deposition peak to move into the region past the O-point, as shown in figure 10. We are now beginning to see the shadowing effect. In stage (*d*), shown in figure 11, the shadowing effect reduces the steady-state island temperature u_0 below its linear model prediction u_0^{lin} and results in $A < 1$.

In addition to the amplification of u_0 relative to u_0^{lin}, the asymmetry of the u_0 curve compared to the u_0^{lin} curve seen in figure 6 may serve as an additional experimental signature of the nonlinear effect. However, the extent to which the asymmetry is present can be strongly affected by the microinstability threshold.

7. Calculations for ASDEX Upgrade (AUG)

7To study the non-linear effect in RF rays launched from the low-field side, we conducted additional simulations for the stabilization of $q = 3/2, 15\%$ and $q = 2, 25\%$ islands at $t = 3400$ and $t = 5400$ ms in the AUG shot 35 350. The profiles and plasma cross-section at these two times are shown in figure 12. The solid blue lines indicate the edges of the regions subtended by the islands, and the solid green lines indicate the locations of the rational surfaces. The red '+' signs indicate the locations of the EC launchers. The vertical orange lines indicate the position of the second harmonic EC resonance.

AUG has 8 EC launchers on the low field side of the plasma, located at major radii R ranging from $R = 2.312$ to $R = 2.38$, at $z = \pm 0.32$ and $z = 0$, and at 4 different azimuthal angles, ϕ [45]. All AUG launchers have steerable mirrors. The poloidal launch angle ranges are sufficient to cover the entire core plasma. The toroidal launch angle ranges are $\alpha = 180^\circ \pm 25^\circ$. This is sufficient to cover the region where the current drive efficiency is maximized. The range of α is to be contrasted with the toroidal launch angle for the DIII-D top launch experiments, which is 61° relative to the $-\hat{R}$ direction.

The islands were taken to be rotating for the AUG calculations reported here. For simplicity, and to accelerate the calculations, the AUG calculations assume that there is a single ray originating from the launcher at $R = 2.364$, $z = 0.32$, $\phi = 98.46^\circ$. The diffusivity was taken to be a constant, with $\kappa_\perp = 0.1\,\mathrm{m^2\,s^{-1}}$. The injected EC power was taken to be 1MW. The calculated driven EC current is shown as a function of the poloidal launch angle for several different values of the toroidal launch angle in figure 14. The current drive efficiency peaks at $\alpha \approx 180^\circ \pm 20^\circ$.

Figure 13 shows the calculated amplification as a function of the poloidal launch angle for several different values of the toroidal launch angle. Values of amplification up to $A \approx 1.8$ are seen. The highest amplification is seen at the toroidal launch angles having the largest distance from $\alpha = 180^\circ$, and for the launchers that are off the midplane. It can be seen in figure 13 that the amplification is increasing very rapidly as the largest toroidal launch angles are approached.

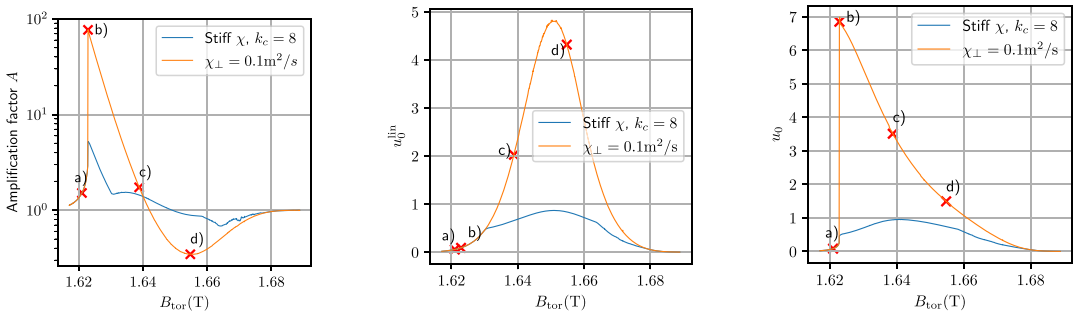

Figure 6. Stages in a B_{tor} sweep, run with locked 25% islands and $P = 1$MW. Compare the constant and stiff $\kappa_\perp$ traces. Note that the stiffness threshold limits island heating and saturates the non-linear effect.

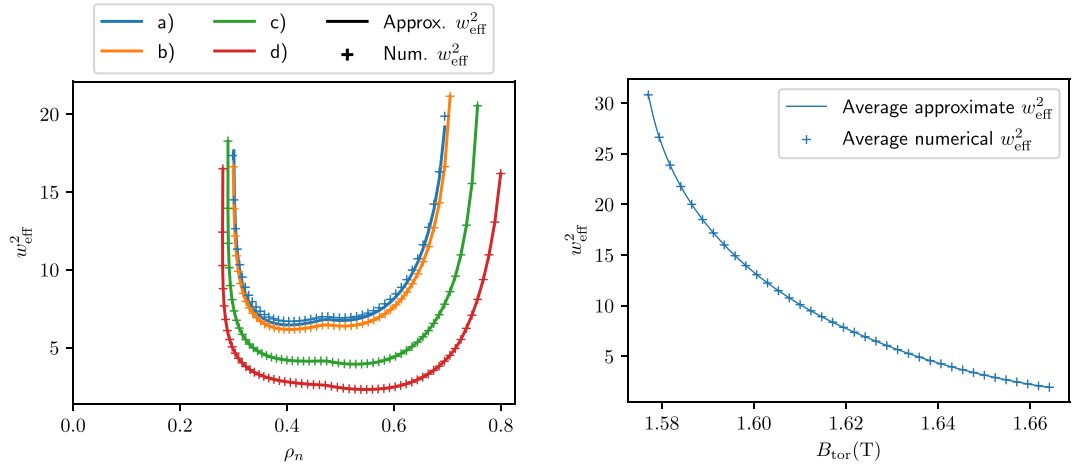

(a) The numerical and approximate w_{eff}^2 along the trajectories of case (a) through (d) in Fig. 6.

(b) Trajectory-averaged numerical and approximate w_{eff}^2 across the B_{tor} sweep in Fig. 6.

Figure 7. Comparison between numerical and approximate w_{eff}^2.

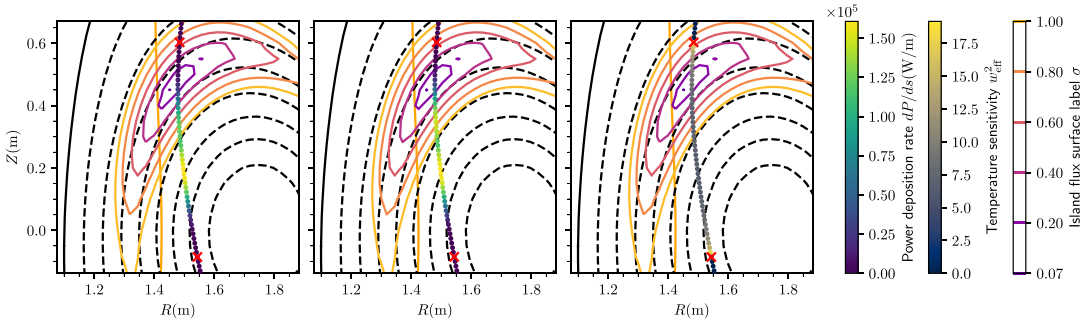

Figure 8. From left to right, the $(\mathrm{d}P/\mathrm{d}s)_{\mathrm{lin}}$, amplified $\mathrm{d}P/\mathrm{d}s$, and w_{eff}^2 in the rising stage of a B_{tor} scan. (point (*a*) in figure 6).

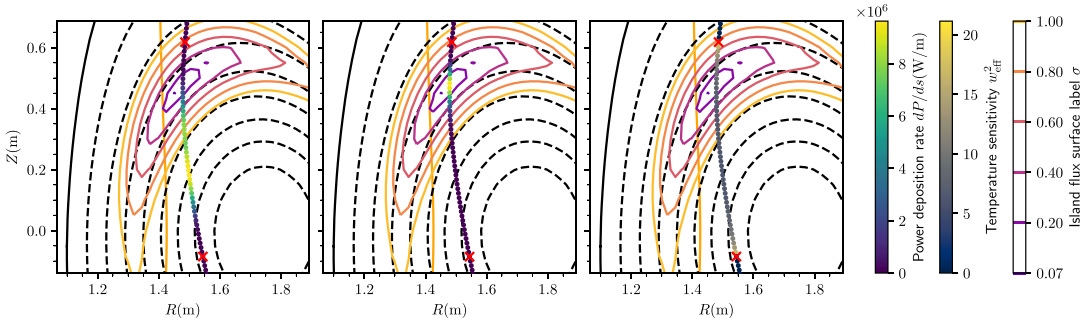

Figure 9. From left to right, the $(\mathrm{d}P/\mathrm{d}s)_{\rm lin}$, amplified $\mathrm{d}P/\mathrm{d}s$, and $w_{\rm eff}^2$ at the A maximum of a $B_{\rm tor}$ scan. (point (b) in figure 6).

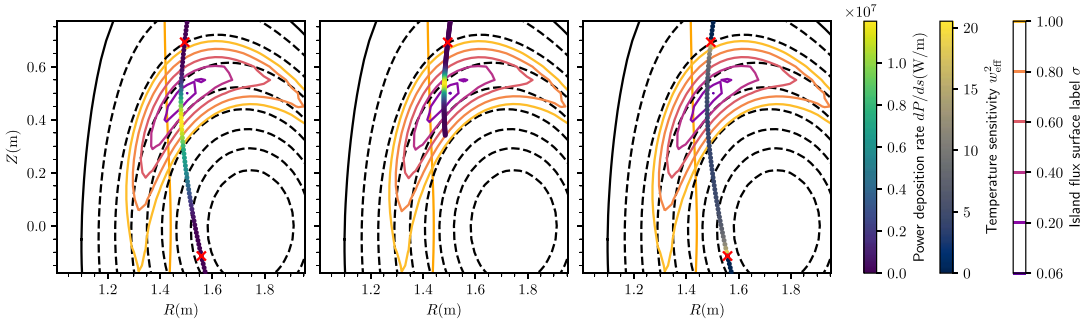

Figure 10. From left to right, the $(\mathrm{d}P/\mathrm{d}s)_{\rm lin}$, amplified $\mathrm{d}P/\mathrm{d}s$, and $w_{\rm eff}^2$ in the falling stage of a $B_{\rm tor}$ scan. Note that the ray's $\mathrm{d}P/\mathrm{d}s$ maximum occurs before reaching the O-point (point (c) in figure 6).

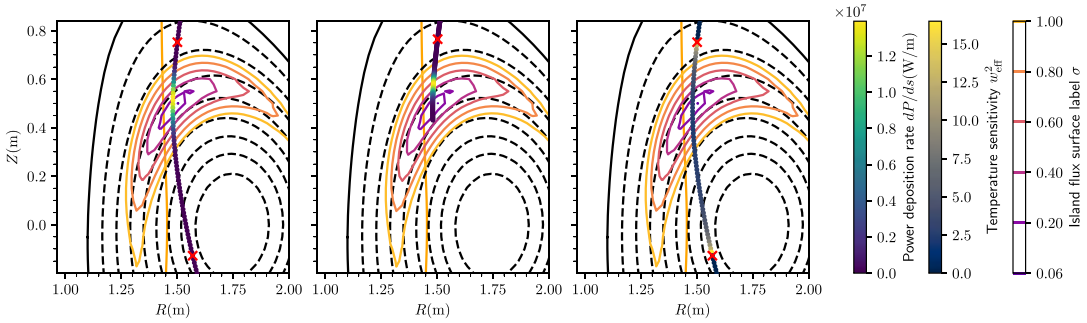

Figure 11. From left to right, the $(\mathrm{d}P/\mathrm{d}s)_{\rm lin}$, amplified $\mathrm{d}P/\mathrm{d}s$, and $w_{\rm eff}^2$ at the A minimum of a $B_{\rm tor}$ scan. Note the strong shadowing effect. (point (d) in figure 6).

8. Conditions governing the magnitude of the nonlinear effects

Significant non-linear effects can be seen when the power deposition and consequent heating of the plasma along an EC ray trajectory causes the power deposition profile to shift earlier along the trajectory. When the ray trajectory passes through a large, heated island, there is a local maximum in the temperature profile in the interior of the island. This can lead to coalescence of the power deposition near the temperature maximum. The shift of the power deposition location is constrained by the relativistic constraint discussed in section 2.1, which limits the region where the EC power may be deposited. RF condensation is most readily seen when damping is permitted at the local temperature maximum in the island interior, and in a significant portion of the ray trajectory lying in the island region beyond the temperature maximum. The nonlinearity can also lead to a shadowing effect, in which the power is deposited before the temperature maximum is reached. The relativistic constraint can be helpful here if it limits the region where the power can be deposited before the temperature maximum is reached.

As discussed in section 2.1, the strength of the nonlinear effects also depends on the value of $w_{\rm eff}$. Figure 15(a)

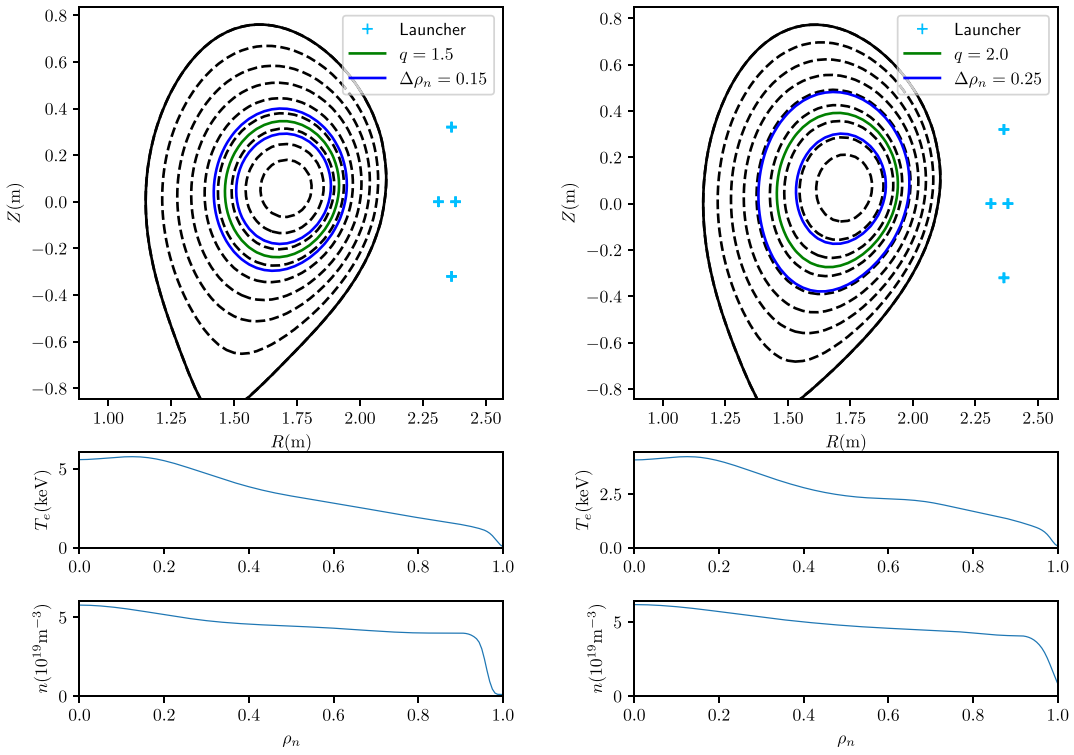

(a) $t = 3400ms, q = 3/2, 15\%$ island (b) $t = 5400ms, q = 2, 25\%$ island

Figure 12. Equilibrium and profiles for AUG shot 35 350, at two chosen times.

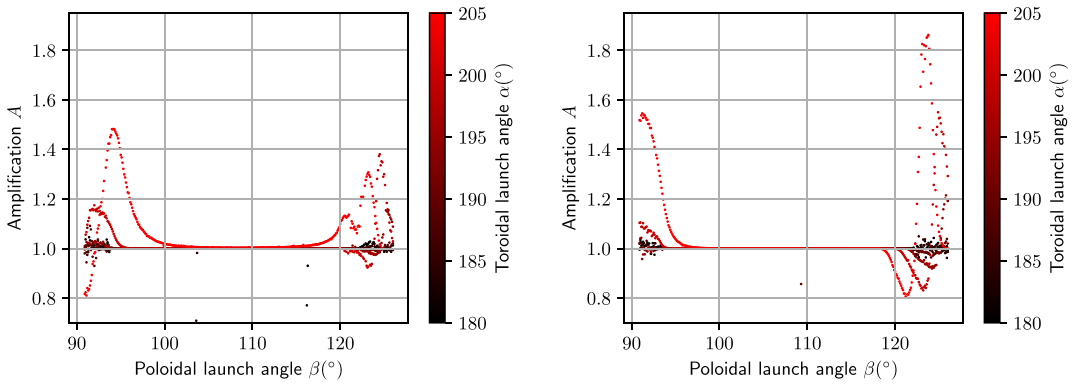

(a) $t = 3400$ms (b) $t = 5400$ms

Figure 13. Amplification A with 1MW EC power in AUG shot 35 350.

shows a top launch ray trajectory and an outside launched ray trajectory in DIII-D as a function of ω/Ω and $N_\parallel$, with the color coding indicating the values of w^2_{eff} and $\mathrm{d}P/\mathrm{d}s$. Here w^2_{eff} has been evaluated using an approximate analytic formula, as discussed in appendix B. The trajectories correspond to the maximum amplification points in two B_{tor} scans, as indicated in figure 15(*b*). Only the portions of the trajectories that lie in the island are shown in the figure. The top launch ray trajectory is the same as that shown in figure 1. That trajectory turns around in the island interior, exits the island, and then crosses the island chain again.

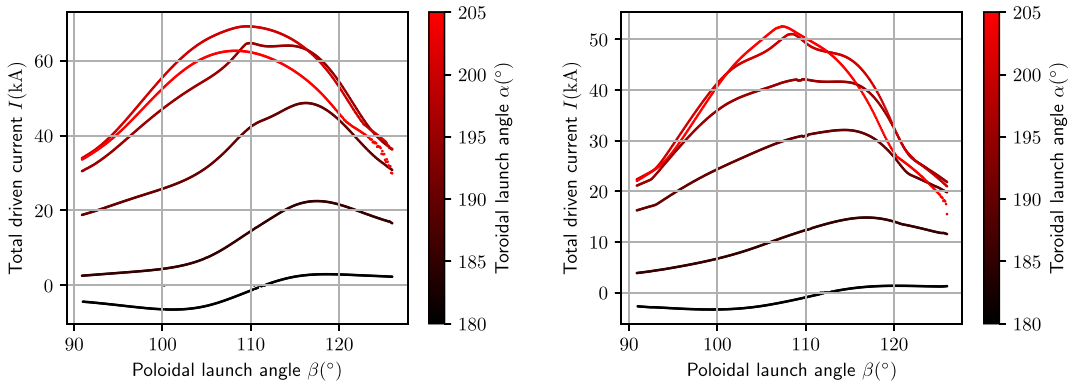

(a) $t = 3400$ms (b) $t = 5400$ms

Figure 14. Total EC-driven current I with 1MW EC power in AUG shot 35 350.

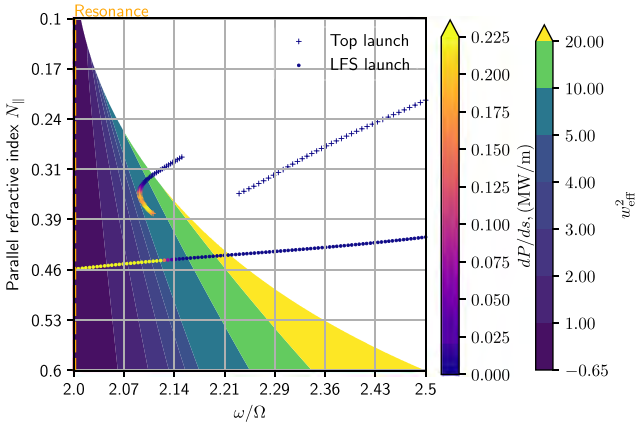

(a) DIII-D $w^2_{eff}(T_0, N_\parallel, \omega/\Omega)$, with in-island ray trajectory and deposition rate. $N_\parallel$ depends on the ray's alignment with magnetic field. $\omega/\Omega \propto R$ through Ω. T_0 is the unmodified, unperturbed island temperature. The left edge of the plot, $\omega/\Omega = 2$, is the resonance.

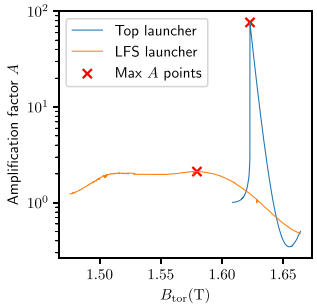

(b) Comparison of A between top and LFS launch, calculated with constant $\chi_\perp$. The two crosses correspond to the two cases with maximum A in 15a.

Figure 15. Comparison of $w^2_{\rm eff}$, in-island trajectories and deposition rate(left) at max A cases (highlighted in right) for top and low field side launchers. Note that the ray from the top launcher does not damp completely, and crosses the island chain again. The simulation is run with constant $\kappa_\perp = 0.1\,\mathrm{m^2\,s^{-1}}$ and $P = 1$MW.

For $\omega/\Omega > 2$, $w^2_{\rm eff}$ monotonically increases with $\omega/\Omega \propto R$. Relative to the trajectory launched from the low field side, the top launch trajectory spends more of its time in a region farther from the second harmonic resonance and is absorbed at higher $w^2_{\rm eff}$.

It can also be seen in figure 15(*a*) that $N_\parallel$ is larger along the top launch ray trajectory. Equation (3) shows that the width of the allowed power deposition region, as determined by relativistic effects, is larger when $N^2_\parallel$ is larger. The value of $N^2_\parallel$ at the launching point is determined mainly by the toroidal launch angle and is larger when the toroidal launch angle is larger.

9. Discussion

Calculations in recent years have suggested that nonlinear effects can significantly impact the stabilization of magnetic islands by RF-driven currents [16–24]. The effects can potentially be used to improve stabilization efficiency. If not properly accounted for in the aiming of ray trajectories, they may lead to a shadowing effect that impairs stabilization. Calculations also suggest that a broad RF-driven current in a fusion reactor could provide automatic stabilization of tearing modes, with the RF-driven current coalescing in a magnetic island when the island reaches sufficient width.

This paper presents a set of simulations investigating the conditions under which RF condensation might be encountered in present-day tokamaks. Quantitative validation of the theory predicting RF condensation has been lacking, and the simulation results illuminate the conditions required for experimental validation of the theory of RF condensation. The paper has focused primarily, but not exclusively, on EC waves launched from above the plasma (top launch). Top launch provides increased ECCD efficiency relative to outside launch, [39, 40] and is, therefore, more likely to be used for a fusion reactor, where recirculating power can have a major impact on the cost of electricity. Top launch ECCD is also most efficient at large toroidal launch angles, where nonlinear effects are most pronounced. Outside launch ECCD (launched from the low field side of the plasma), in contrast, is most efficient at intermediate toroidal launch angles. In the AUG calculations described here, the current drive efficiency peaks at the toroidal launch angles of about 20° relative to the $-\hat{R}$ direction. The largest possible toroidal launch angle for the AUG launchers relative to the $-\hat{R}$ direction is about 25°. In contrast, the toroidal launch angle relative to $-\hat{R}$ in the DIII-D top launch experiments was 61° .

ECCD island stabilization experiments have thus far largely been done using outside launch, with toroidal launch angles that maximize the current drive efficiency. The AUG calculations described in this paper find that the nonlinear effects are predicted to be weak for such toroidal launch angles. It is not surprising, then, that the nonlinear effects discussed in this paper have not made themselves known in the analysis of such experiments, although Bardoczi and Logan have reported seeing a signature of RF condensation [46]. In a reactor with top launch ECCD, the nonlinear effects are predicted to be more significant.

Our work shows that, in the DIII-D calculations, the combined effects of stiffness above the microinstability threshold and rotation can lead to a muted and more gradual onset of the nonlinear effects. With an increased fraction of the power deposited in the island periphery, the local microinstability threshold is encountered first in the peripheral region, with the boundary of the stiff region moving gradually inward. The temperature increase in the island is more gradual. There is no indication that a bifurcation threshold is being approached.

These calculations may overstate the effect of stiffness. With a flat density profile, it would be expected that the ITG threshold will be encountered when the ion temperature gradient becomes sufficiently large. There is evidence that this would affect the ion temperature gradient directly but would only affect the electron temperature gradient through the coupling of the electrons to the ions. It has been found on both W7X and AUG that, for a plasma heated by ECH, the ion temperature is clamped when it reaches the ITG threshold, but the electron temperature can significantly exceed the ion temperature, depending on the coupling between the electrons and the ions [47, 48]. Calculations of these two-fluid effects are beyond the scope of this paper.

The picture of the combined impact of rotation and stiffness suggests that, for rotating islands, it may be advantageous to use modulated ECCD to deposit the power more effectively in the central portion of the island and retain some of the advantages that are seen with locked islands. In particular, in a validation experiment, locking may pose a problem for ECE measurements, depending on the location of the line of sight of the ECE diagnostic relative to the EC launchers. It may be preferable to prevent the island from locking by feed-forward entrainment in a rotating resonant magnetic perturbation [26]. For a rotating island, it will be of interest to calculate the predicted impact on the nonlinear effects of modulation with various duty cycles. These calculations are beyond the scope of this paper.

For a fusion reactor with a broad RF-driven current, the conventional linear theory of the stabilization of islands via unmodulated ECCD predicts little or no stabilization of islands unless the aiming of the RF is appropriately adjusted by external feedback control. The linear stabilization effect relies on a current density gradient across the island that decreases from the island center radially outward. There is a geometric effect such that the equilibration of this current along magnetic field lines yields a stabilizing resonant component of the current density. The nonlinear RF condensation effect would, however, automatically lead to the coalescence of the ECCD in the island, producing a stabilizing resonant component of the field without the need for feedback control. As described above, depending on the strength of the coupling between the ions and electrons (i.e. depending on the density and temperature), the combined effects of stiffness and rotation may lead to a muted and gradual onset of the nonlinear effects. The nonlinear effect may nevertheless be sufficient to stabilize the island. Prediction of the magnitude of the stabilizing resonant current in this case will require the application of a quantitative model that has been benchmarked against experimental data. This paper has investigated possible scenarios for providing that benchmarking.

The stabilization could be improved by modulating the ECCD with a frequency and phase determined by the Mirnov oscillations as soon as such oscillations are detected. That would require an increased level of EC power in order to produce the same current density as the unmodulated EC. A broad ECCD profile would then provide some linear stabilization, and the stabilization could be enhanced by a condensation effect that is comparable to that for a locked island.

A growing island that is not stabilized in a fusion reactor will likely lock to the wall at a relatively small island width. Future large tokamaks are expected to rotate much more slowly than DIII-D or AUG, and the islands are expected to lock at correspondingly smaller widths. It has been projected that the $q = 2$ island in the ITER base case will lock at a width of less than 5% of the minor radius [49]. ECCD stabilization of locked islands has been demonstrated in a series of experiments on DIII-D by Volpe *et al* [25]. To stabilize locked islands, it will be necessary for the islands to lock at a phase where the EC launcher is approximately aligned with the island O-point [23]. This can be arranged by a proper adjustment of the field error compensation coils. As in contemporary tokamaks, ITER will have field error compensation coils that substantially reduce the magnitude of undesirable nonaxisymmetric resonant components of the magnetic field produced by

finite tolerances in the placement of the magnetic field coils. It is expected that future large tokamaks will also have such coils. The phase of locked islands will be determined by the residual resonant components of the field after partial cancellation. A slight adjustment of the field produced by the field error correction coils, produced by a slight adjustment in the relative magnitudes of the currents in the coils, will be sufficient to lock the islands at the desired phase. If the island is locked at the appropriate phase, a broad ECCD profile would then produce a linear stabilizing effect, which would be enhanced by RF condensation.

The theory describing the EC power deposition and current drive in a plasma with a given temperature and density has been well validated [33]. This paper has therefore focused on the temperature perturbation in the island produced by a given level of power deposition, and the resulting nonlinear enhancement of the power deposition. This depends on heat transport in the island, for which there is at present only a limited quantitative understanding. There is strong evidence that the cross-field heat transport in the island is small relative to the turbulent heat transport outside the island when the temperature gradient in the island is sufficiently small [34–37]. It is presumed that the heat transport in the island rises to the same level as that outside the island when the temperature gradient in the island gets sufficiently large. There is at present only a limited quantitative understanding of this transition. Experiments investigating RF condensation would also provide information on that issue.

Although we have focused on the issue of the nonlinearly enhanced temperature perturbation in this paper, we are ultimately interested in that effect for the purpose of stabilizing islands via RF-driven currents. That stabilizing effect is stronger than might be surmised by considering only the temperature perturbation. If the temperature perturbation increases with increasing EC power until it reaches a critical temperature gradient above which the temperature profile in the island becomes stiff, the EC-driven current will nonetheless continue to increase with increasing EC power. Any nonlinear narrowing of the power deposition profile that occurs below the temperature gradient threshold will continue to be reflected in the current density profile as the driven current increases further. For a broad EC current profile, the helical perturbation of the temperature profile will continue to be reflected in a resonant perturbation of the current density, with the amplitude of that resonant current density perturbation continuing to increase in proportion to any further increase in the EC power even if the temperature perturbation is clamped by profile stiffness.

Acknowledgments

Work supported by DOE Contracts DE-SC0023236, DE-AC02-09CH11466, and DE-FG02-97ER54415. This material is based upon work supported by the U.S. Department of Energy, Office of Science, Office of Fusion Energy Sciences, using the DIII-D National Fusion Facility, a DOE Office of Science user facility, under Award(s) DE-FC02-04ER54698, DE-AC52-07NA27344, and DE-SC0022270.

This work has been carried out within the framework of the EUROfusion Consortium, funded by the European Union via the Euratom Research and Training Programme (Grant Agreement No 101052200—EUROfusion). Views and opinions expressed are however those of the author(s) only and do not necessarily reflect those of the European Union or the European Commission. Neither the European Union nor the European Commission can be held responsible for them.

Disclaimer

Appendix A. Table of quantities

Table 1. A table of important quantities.

Symbol	Definition
P_{dep} (W)	Power deposition.
V_p	The phase velocity of the x-mode waves.
V_T	The thermal velocity of the electrons.
w	The sensitivity of damping to temperature. $w = \frac{V_p}{V_T}$.
w_{eff}	w before the temperature perturbation. See B for more discussions.
κ_0 ($\text{m}^2\,\text{s}^{-1}$)	The thermal diffusivity below the ITG threshold. See (5)
κ_s ($\text{m}^2\,\text{s}^{-1}$)	The thermal diffusivity above the ITG threshold. See (5)
k_c	The normalized ITG threshold. See (5)
σ	An island flux surface coordinate. Ranges from 0 to 1 from the o-point to the separatrix.
u	The normalized island temperature. $u = \frac{(T-T_s)}{T_s}$. T_s is the separatrix temperature.
u_0^{lin}	The normalized island o-point temperature, according to the linear model.
u_0	The normalized island o-point temperature, with RF condensation.
A	The amplification factor due to RF condensation. $A = \frac{u_0}{u_0^{\text{lin}}}$
B_{tor} (T)	The vacuum toroidal field at the magnetic axis.
α	The toroidal launch angle.
β	The poloidal launch angle.

Appendix B. Approximate w_{eff}^2 formula and its accuracy

The w_{eff}^2 values presented in this paper are approximate values [23] given by:

$$-w_{\text{eff}}^2 = \mu\left(1 - \frac{2\Omega/\omega}{1-N_\parallel^2}\right) + \frac{\xi_2 I_{3/2}(\xi_2)}{I_{5/2}(\xi_2)} - \frac{5}{2}, \tag{8}$$

where

$$R_2 = \sqrt{\left(\frac{2\Omega}{\omega}\right)^2 - 1 + N_\parallel^2}, \tag{9}$$

and

$$\xi_2 = \frac{N_\parallel R_2 \mu}{1-N_\parallel^2}. \tag{10}$$

Using the cases with scaled B_{tor} in (8), we show that the formula closely approximates the numerical values evaluated using $w_{\text{eff}}^2 \equiv T\partial_T[ln(dP_{lin}/ds)]$ using finite differences.

ORCID iDs

Lanke Fu https://orcid.org/0000-0002-6845-387X
E. Litvinova Mitra https://orcid.org/0000-0001-8345-6449
A.H. Reiman https://orcid.org/0000-0002-9876-7351
L. Bardoczi https://orcid.org/0000-0002-8280-2423
Xi Chen https://orcid.org/0000-0002-8718-6877
W. Choi https://orcid.org/0000-0002-6891-2300
N.J. Fisch https://orcid.org/0000-0002-0301-7380
Q. Hu https://orcid.org/0000-0002-8877-4988
E. Jung https://orcid.org/0000-0001-5108-8055
M. Maraschek https://orcid.org/0000-0002-3246-7559
J.J. McClenaghan https://orcid.org/0000-0003-4735-0991
E. Strait https://orcid.org/0000-0001-9215-3757
J. Yang https://orcid.org/0000-0001-8422-8464

References

[1] Gerasimov S.N. *et al* 2020 Overview of disruptions with JET-ILW *Nucl. Fusion* **60** 066028
[2] de Vries P.C. *et al* 2014 *Phys. Plasmas* **21** 056101
[3] de Vries P.C. *et al* 2016 *Nucl. Fusion* **56** 026007
[4] Nathaniel J.F. 1978 Confining a tokamak plasma with rf-driven currents *Phys. Rev. Lett.* **41** 873–6
[5] Fisch N.J. and Boozer A.H. 1980 Creating an asymmetric plasma resistivity with waves *Phys. Rev. Lett.* **45** 720–2
[6] Reiman A.H. 1983 *Phys. Fluids* **26** 1338
[7] Yoshioka Y., Kinoshha S. and Kobayashi T. 1984 Numerical study of magnetic island suppression by RF waves in large tokamaks *Nucl. Fusion* **24** 565
[8] Gantenbein G., Zohm H., Giruzzi G., Günter S., Leuterer F., Maraschek M., Meskat J. and Yu Q. (ASDEX Upgrade Team and ECRH-Group (AUG)) 2000 Complete suppression of neoclassical tearing modes with current drive at the electron-cyclotron-resonance frequency in ASDEX upgrade tokamak *Phys. Rev. Lett.* **85** 1242–5
[9] Zohm H. *et al* 2001 The physics of neoclassical tearing modes and their stabilization by ECCD in ASDEX upgrade *Nucl. Fusion* **41** 197
[10] Zohm H. *et al* (ASDEX Upgrade Team) 2001 *Phys. Plasmas* **8** 2009
[11] Leuterer F. *et al* 2003 Recent ecrh results in ASDEX upgrade *Nucl. Fusion* **43** 1329–42
[12] La Haye R.J., Günter S., Humphreys D.A., Lohr J., Luce T.C., Maraschek M.E., Petty C.C., Prater R., Scoville J.T. and Strait E.J. 2002 Control of neoclassical tearing modes in diii-d *Phys. Plasmas* **9** 2051–60
[13] Prater R. , Haye R.J.L., Lohr J., Luce T.C., Petty C.C., Ferron J.R., Humphreys D.A., Strait E.J., Perkins F.W. and Harvey R.W. 2003 Discharge improvement through control of neoclassical tearing modes by localized eccd in DIII-D *Nucl. Fusion* **43** 1128

[14] Isayama A. , Kamada Y., Ide S., Hamamatsu K., Oikawa T., Suzuki T., Neyatani Y., Ozeki T., Ikeda Y. and Kajiwara K. 2000 Complete stabilization of a tearing mode in steady state high-β_p h-mode discharges by the first harmonic electron cyclotron heating/current drive on jt-60u *Plasma Phys. Control. Fusion* **42** L37
[15] Isayama A. *et al* 2003 Achievement of high fusion triple product, steady-state sustainment and real-time ntm stabilization in high- $_p$ ELMy H-mode discharges in JT-60U *Nucl. Fusion* **43** 1272–8
[16] Reiman A.H. and Fisch N.J. 2018 Suppression of tearing modes by radio frequency current condensation *Phys. Rev. Lett.* **121** 225001
[17] Rodríguez E., Reiman A.H. and Fisch N.J. 2019 Rf current condensation in magnetic islands and associated hysteresis phenomena *Phys. Plasmas* **26** 092511
[18] Rodríguez E., Reiman A.H. and Fisch N.J. 2020 Rf current condensation in the presence of turbulent enhanced transport *Phys. Plasmas* **27** 042306
[19] Jin S., Fisch N.J. and Reiman A.H. 2020 Pulsed rf schemes for tearing mode stabilization *Phys. Plasmas* **27** 062508
[20] Frank S.J., Reiman A.H., Fisch N.J. and Bonoli P.T. 2020 Generation of localized lower-hybrid current drive by temperature perturbations *Nucl. Fusion* **60** 096027
[21] Reiman A.H., Bertelli N. Fisch N.J., Frank S.J., Jin S., Nies R. and Rodriguez E. 2021 Disruption avoidance via radio frequency current condensation in magnetic islands produced by off-normal events *Phys. Plasmas* **28** 042508
[22] Jin S., Reiman A.H. and Fisch N.J. 2021 Two-fluid model of rf current condensation in magnetic islands *Phys. Plasmas* **28** 052503
[23] Nies R., Reiman A.H., Rodriguez E., Bertelli N. and Fisch N.J. 2020 Calculating rf current condensation with consistent ray-tracing and island heating *Phys. Plasmas* **27** 092503
[24] Jin S., Reiman A.H. and Fisch N.J. 2021 on the merit of hot ion mode for tearing *Phys. Plasmas* **28** 082509
[25] Volpe F.A., Hyatt A., La Haye R.J., Lanctot M.J., Lohr J., Prater R., Strait E.J. and Welander A. 2015 Avoiding tokamak disruptions by applying static magnetic fields that align locked modes with stabilizing wave-driven currents *Phys. Rev. Lett.* **115** 175002
[26] Choi W., La Haye R.J., Lanctot M.J., Olofsson K.E.J., Strait E.J., Sweeney R. and Volpe F.A. (The DIII-D Team) 2018 Feedforward and feedback control of locked mode phase and rotation in DIII-D with application to modulated eccd experiments *Nucl. Fusion* **58** 036022
[27] Petty C.C., La Haye R.J., Luce T.C., Humphreys D.A., Hyatt A.W., Lohr J., Prater R., Strait E.J. and Wade M.R. 2004 Complete suppression of the m = 2/ n = 1 neoclassical tearing mode using electron cyclotron current drive in DIII-D *Nucl. Fusion* **44** 243–51
[28] Bardóczi L., La Haye R.J., Strait E.J., Logan N.C., Smith S.P., Richner N.J. and Callen J.D. 2023 Direct preemptive stabilization of m,n = 2,1 neoclassical tearing modes by electron cyclotron current drive in the DIII-D low-torque iter baseline scenario *Nucl. Fusion* **63** 096021
[29] Prater R. *et al* 2007 Stabilization and prevention of the 2/1 neoclassical tearing mode for improved performance in DIII-D *Nucl. Fusion* **47** 371–7
[30] Frank S.J. *et al* 2022 *Nucl. Fusion* **62** 126036
[31] Reiman A. 2016 *Phys. Plasmas* **23** 072502
[32] Smirnov A.P., Harvey R. and Kupfer K. 1994 A general ray tracing code genray *Bull Am. Phys. Soc.* **39** 1626
[33] Prater R. 2004 Heating and current drive by electron cyclotron waves *Phys. Plasmas* **11** 2349–76
[34] Inagaki S., Tamura N., Ida K., Nagayama Y., Kawahata K., Sudo S., Morisaki T., Tanaka K. and Tokuzawa T. 2004 Observation of reduced heat transport inside the magnetic island o point in the large helical device *Phys. Rev. Lett.* **92** 055002
[35] Spakman G.W. *et al* 2008 *Nucl. Fusion* **48** 115005
[36] Bardóczi L., Rhodes T.L., Carter T.A., Crocker N.A., Peebles W.A. and Grierson B.A. 2016 Non-perturbative measurement of cross-field thermal diffusivity reduction at the o-point of 2/1 neoclassical tearing mode islands in the DIII-D tokamak *Phys. Plasmas* **23** 052507
[37] Hornsby W.A., Siccinio M., Peeters A.G., Poli E., Snodin A.P., Casson F.J., Camenen Y. and Szepesi G. 2011 *Plasma Phys. Control. Fusion* **53** 054008
[38] Garbet X. *et al* 2004 Profile stiffness and global confinement *Plasma Phys. Control. Fusion* **46** 1351–73
[39] Xi Chen C.C.P. *et al* 2020 Doubling the efficiency of off-axis current drive using reactor-relevant 'top launch eccd'on the DIII-D tokamak *28th IAEA Fusion Energy Conf., Nice* (*Virtual*, *10–15 May 2021*) (IAEA) pp 10–16 (available at: https://conferences.iaea.org/event/214/)
[40] Xi Chen C.C.P. *et al* 2022 Doubling off-axis electron cyclotron current drive efficiency via velocity space engineering *Nucl. Fusion* **62** 054001
[41] Lao L.L., John H.S., Stambaugh R., Kellman A. and Pfeiffer W. 1985 Reconstruction of current profile parameters and plasma shapes in tokamaks *Nucl. Fusion* **25** 1611
[42] Bardóczi L., Carter T.A., La Haye R.J., Rhodes T.L. and McKee G.R. 2017 Impact of neoclassical tearing mode-turbulence multi-scale interaction in global confinement degradation and magnetic island stability *Phys. Plasmas* **24** 122503
[43] Austin M., Ellis R. James R. and Luce T. 1996 Electron temperature measurements from optically gray third harmonic electron cyclotron emission in the DIII-D tokamak *Phys. Plasmas* **3** 3725–31
[44] Jung E., Bardóczi L., Austin M.E., Son S.H. and Reiman A.H. 2024 Reconstruction of magnetic island electron temperature in mixed second and third harmonic electron cyclotron emission conditions *Rev. Sci. Instrum.* **95** 063502
[45] John Lohr Y.A.G. *et al* 2005 The electron cyclotron resonant heating system on the diii-d tokamak *Fusion Sci. Technol.* **48** 1226–37
[46] Bardoczi L. and Logan N.C. 2021 *Nucl. Fusion* **61** 114001
[47] Beurskens M.N.A. *et al* 2021 *Nucl. Fusion* **61** 116072
[48] Beurskens M.N.A. *et al* 2022 *Nucl. Fusion* **62** 16015
[49] La Haye C., Paz-Soldan R. and Liu Y.Q. 2017 *Nucl. Fusion* **57** 014004